CrossMark

Investigation of structural and electrical properties of $ZnMn_2O_4$ synthesized by sol–gel method

Laurel Simon Lobo[1] · A. Ruban Kumar[1]

Abstract In this present study, we have reported the synthesis of $ZnMn_2O_4$, transitional metal oxide by sol–gel method. The structural and morphological properties are confirmed using various characterization techniques namely XRD, FT-IR and SEM with EDX. Dielectric studies of $ZnMn_2O_4$ are measured at the frequency varying from 50 Hz to 5 MHz for the temperature range of 303–573 K. The temperature dependent electrical parameters like impedance and modulus exhibit a strong correlation with the grains, grain boundaries and space charge effects in the synthesized material. Diffusion of oxygen vacancies in the dipoles and defects in the material due to oxygen vacancy complexes are investigated by the activation energy obtained from Arrhenius plot. It was found that the relaxation process was dominated by the hopping mechanism between the Mn^{3+} and Mn^{4+}. Nyquist plot of impedance was attributed to the existence of space charge interface, grain boundary and grain conduction mechanism of the material.

1 Introduction

Nanocrystalline $ZnMn_2O_4$ is an important class of mixed transitional metal oxide with the general formula AB_2O_4. The physical and chemical properties of the transitional metal oxides exhibit a variety of interesting facts due to the accommodation of different cations with one or more oxidation states [1, 2]. Due to this, $ZnMn_2O_4$ have attracted

a great attention to their electronic, optoelectronic, mechanical, electrochemical and semiconducting properties resulting in the prospective applications owing to the field of sensors, specific memory devices, NTC thermistor, lithium ion batteries as an anode and so on [2–5]. Spinel $ZnMn_2O_4$ with its unique electrical property accounts to potential application as negative temperature co-efficient (NTC) thermistor. In general, it has been investigated as a technologically significant functional material due to its semiconducting nature and its applications in the microelectronics as temperature sensors, power sensing terminators, fire detectors for practical devices [6–8]. However in $ZnMn_2O_4$, Zn-site exhibit single oxidation state of Zn^{2+} whereas Mn-site exhibit Mn^{3+} and Mn^{4+}, which attributes to the formation of oxygen vacancy in the material with the variation of temperature and the relaxation process is related to the oxygen vacancy. Depending upon the temperature variation relaxation process exhibits single-ionized, doubly ionized, diffusion of oxygen in complexes, defects formed of oxygen and cation vacancy in the material [9, 10].

Zinc magnetite ($ZnMn_2O_4$) has been synthesized by various methods namely solid state reaction [11] hydrothermal method [2, 3], sol–gel method [1], spin coating [12]. To obtain a homogenous chemical composition, high Crystallinity, uniform particle size and morphology, sol–gel method using microwave assisted sintering technique was used in order to reduce the agglomeration of the material.

In this study, $ZnMn_2O_4$ is synthesized by sol–gel method via glycine as a chelating agent. The properties of the materials are strongly affected by the particle size and morphology. Hence, synthesis of the material in nano range has attracted the researchers deliberately [3, 7]. From literature, spinel $ZnMn_2O_4$ functional material is analysed for

✉ A. Ruban Kumar
arubankumarvit@gmail.com

[1] School of Advanced Sciences, VIT University, Vellore 632014, India

its thermal properties, magnetic properties, optical studies, photoelectrical properties, electrochemical studies for various applications [2–5, 13]. However until date, there were no reports to the best of author's knowledge to understand in-depth analysis of dielectric, impedance and electric modulus on $ZnMn_2O_4$. The electrical properties for the synthesized $ZnMn_2O_4$ as a function of frequency varying from 50 Hz to 5 MHz at different temperatures have been measured. In particular, the contribution of grain, grain boundary and interfacial effects at different temperatures and relaxation process are analyzed. The formation of thermal motion of ions due to the oxygen vacancy in the material corresponds to the hopping mechanism in the Mn-site, i.e., Mn^{3+} and Mn^{4+} during temperature variation results in the dielectric relaxations in the material.

2 Experimental

$ZnMn_2O_4$ microspheres were synthesized by sol–gel method using glycine as a chelating agent. The stoichiometric ratio of zinc acetate dihydrate $[(CH_3COO)_2Zn·2H_2O]$, and manganese acetate tetrahydrate $[(CH_3COO)_2Mn·4H_2O]$ dissolved in the deionized water and glycine solution was added slowly drop by drop to it, which acts as a chelating agent. All reagents used were of analytical grade and used without further purification. The solution was stirred continuously for 3 h at room temperature. Further, the homogenous solution was heated to 80 °C with stirring to ensure homogeneity until the gel was formed. The obtained gel was dried overnight in a vacuum oven at 120 °C. The gel precursors were decomposed at 300 °C for 5 h to eliminate the organic constituents present. Finally, the decomposed powder was slightly ground and sintered in the microwave furnace at 850 °C for 3 h. Again the obtained $ZnMn_2O_4$ was ground into fine powder before subjecting it to further analysis.

The phase formation of the synthesized material were investigated by X-ray diffraction (XRD, Brucker D8 Advance, Cu Kα radiation, λ = 1.5406 Å) with a range of 2θ from 10° to 80° with a step size of 0.02 s^{-1} at a scan rate of 2 min^{-1}. The Fourier transform infrared spectroscopy (FT-IR) spectra obtained by JASCO 400 Infrared spectrometer from 4000 to 400 cm^{-1}. The surface morphology and compositions of the samples investigated by scanning electron microscopy (Carl Zeiss EVO-185H, UK) equipped with an energy-dispersive X-ray spectrometer (EDX). The synthesized $ZnMn_2O_4$ powder converted to cylindrical pellets for electrical measurements by coating with the silver paste for ohmic contact. The dielectric measurements were carried out by an LCR meter (HIOKI 3532-50LCR meter HITESTER) in the frequency range from 50 Hz to 5 MHz for the temperature ranging from 303 to 573 K.

3 Results and discussion

3.1 Structural and morphological analysis

Figure 1 illustrates the XRD pattern for the synthesized $ZnMn_2O_4$ which attributes to the phase formation and crystal structure. It is observed from the XRD pattern that all the diffraction peaks clearly corresponds to the standard JCPDS 77-0470 with space group I41/amd and hkl values indexed accordingly. XRD peaks were sharp and very intense, indicating the good crystalline nature of the material without any secondary phase formation. The unit cell parameters calculated from PowderX software [14] were a = b = 5.71749 Å and c = 9.23527 Å.

The average particle size of the synthesized $ZnMn_2O_4$ was estimated using the FWHM values of the major peaks in the XRD pattern from Scherrer's formula [15].

$$D = k\lambda/\beta\cos\theta, \tag{1}$$

where D is crystallite size, k = 0.9 is the particle shape factor, λ = 1.5405 Å is the X-ray wavelength used, β is the full-width half maximum of the major XRD peaks, and θ is the Bragg's angle. The average crystallite size was found to be around 55–95 nm.

Figure 2 illustrates the FT-IR spectroscopy recorded in the range of 400–4000 cm^{-1}. It observed strong absorption peak between 500 and 700 cm^{-1} region which corresponds to the formation of metal–oxygen bonds of tetrahedral and octahedral sites i.e. Zn–O and Mn–O bonds. These bands confirm the formation of spinel compounds for the synthesized material [2, 4].

The surface morphology of $ZnMn_2O_4$ SEM images are shown in the Fig. 3. SEM images in Fig. 3a–c observes the agglomerated spherical particles. It is evident that the particles are distributed uniformly in size. The microstructure of
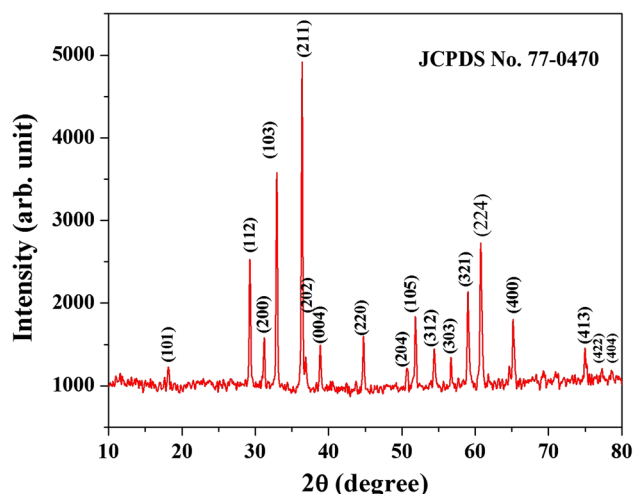
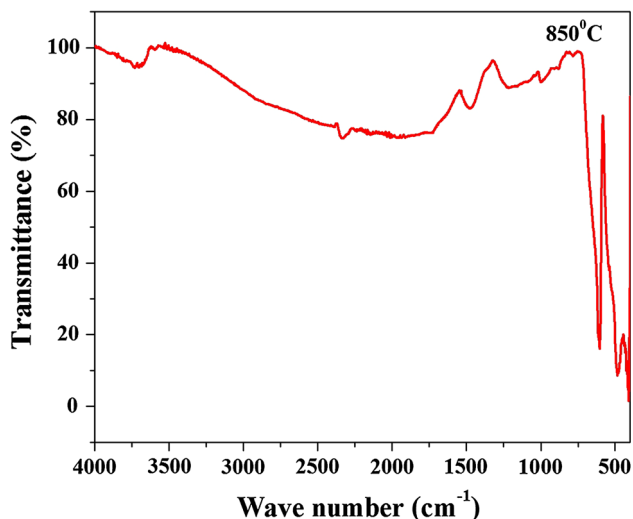**Fig. 1** XRD pattern of as synthesized $ZnMn_2O_4$

Fig. 2 FT-IR spectroscopy of $ZnMn_2O_4$

the sample showed well-defined grains and grain boundaries in the SEM images. The elemental compositions of the sample are obtained from EDX spectrum as shown in Fig. 3d. The EDX spectrum shows the elemental mapping along with the percentage of composition of each element as

shown in the inset of Fig. 3d. It confirms the absence of any impurity in the synthesized sample indicating the formation of exact composition.

3.2 Dielectric studies

The electric parameters such as real part of dielectric constant (ε'), the imaginary part of dielectric constant (ε'') and ac-conductivity were calculated using the equation below.

$$\varepsilon' = Cd/A\varepsilon_0, \tag{2}$$

$$\sigma_{ac} = 2\Pi f\varepsilon'\varepsilon_0\tan\delta \tag{3}$$

and

$$\varepsilon'' = \sigma_{ac}/\varepsilon_0\omega, \tag{4}$$

where C is capacitance in farad, d is the thickness of the pellet in mm, A is cross-sectional area of the pellet in m^2, ε_0 is constant of permittivity in free space, $\omega = 2\pi f$ is the angular frequency, and $\tan\delta$ is dielectric loss [16]. Figure 4a, b shows the variation in the real (ε') and imaginary (ε'') part of dielectric constant obtained using the Eqs. (2) and (4). These values decrease gradually with increase in
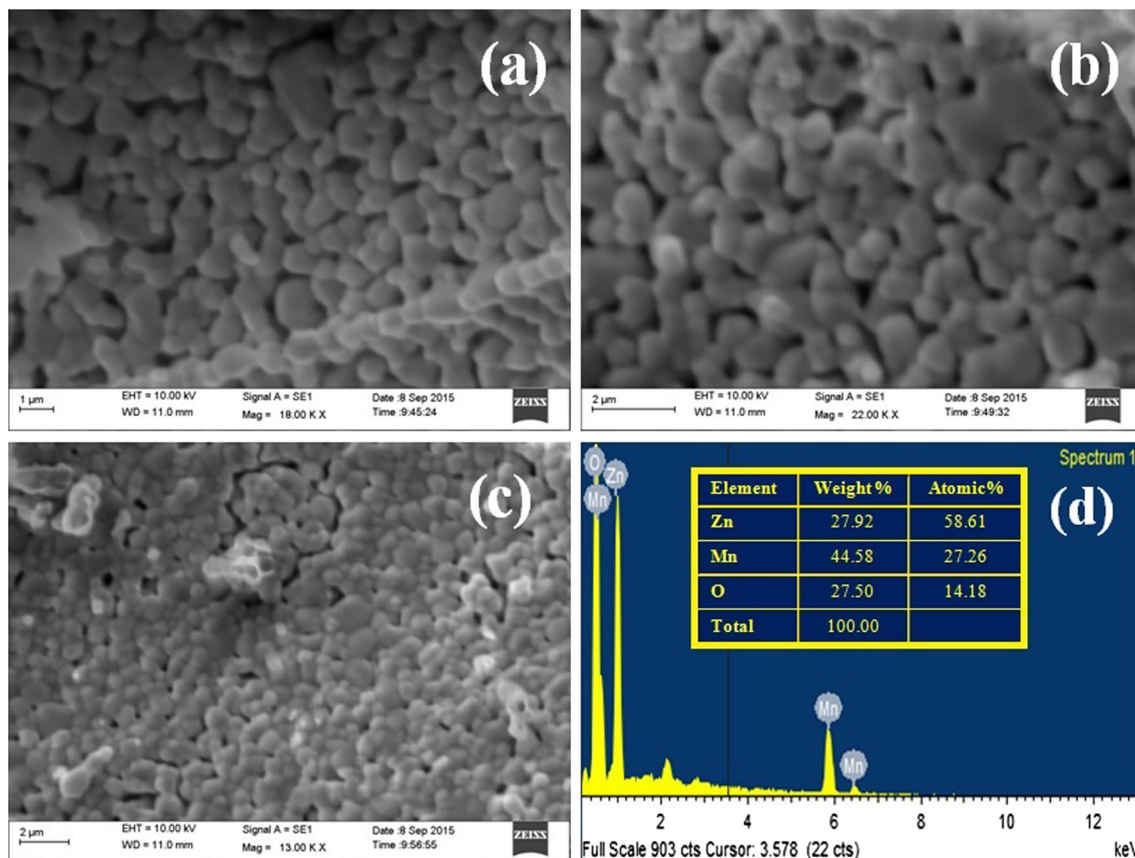

Fig. 3 **a–c** SEM images of different magnifications, **d** EDX spectra, *inset* shows the percentage of chemical compositions of $ZnMn_2O_4$
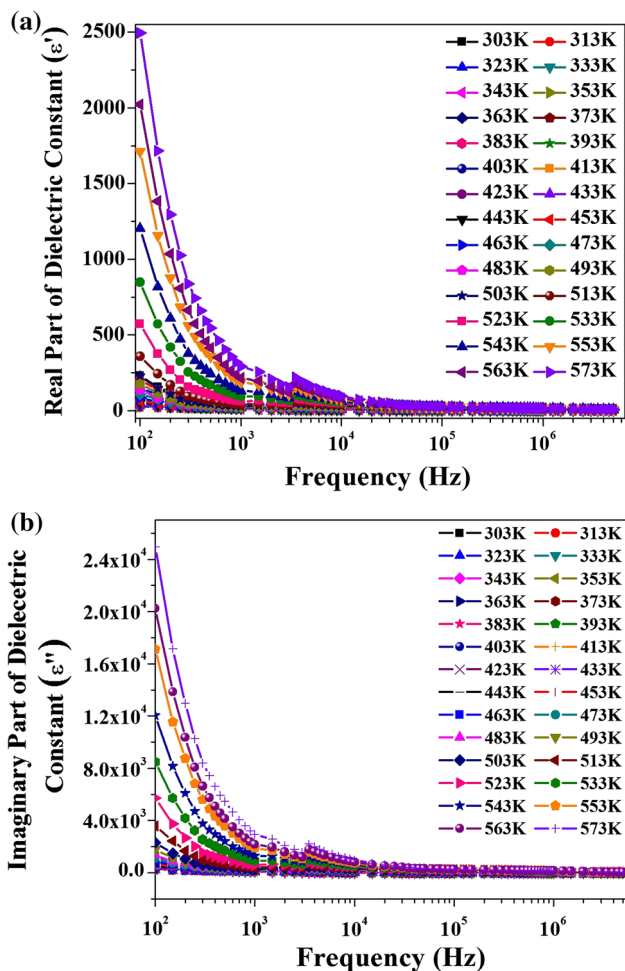
(a)

(b)

Fig. 4 Variation of **a** real (ε′) and **b** imaginary (ε″) part of dielectric constant with frequency for different temperature of ZnMn₂O₄

Fig. 5 Variation of dielectric loss tangent (tan δ) with frequency for different temperature of ZnMn₂O₄

the frequency at low-frequency region whereas it is almost independent of the frequency in the high-frequency region. This type of behaviour is explained by Maxwell–Wagner model [17]. According to this model, highly conducting grains are separated by low conducting grain boundary at lower frequencies [16, 18]. At higher frequencies, piling up of charges at grain boundaries increases resulting in the space charge polarization effect in the material. This pattern of variation in the dielectric constant with frequency is due to the grain boundary, defects, hopping of electrons between Mn^{3+} and Mn^{4+}, oxygen vacancy, space charge polarization effect, voids, etc. At very low frequency, the higher value of dielectric constant with the increase in temperature observed due to the thermal activation of the charges in ZnMn₂O₄.

Figure 5 shows the frequency dependent dielectric loss tangent (tan δ) for different temperatures from 303 to 373 K. As the frequency increases dielectric loss tends to become almost zero and is independent of frequency. At
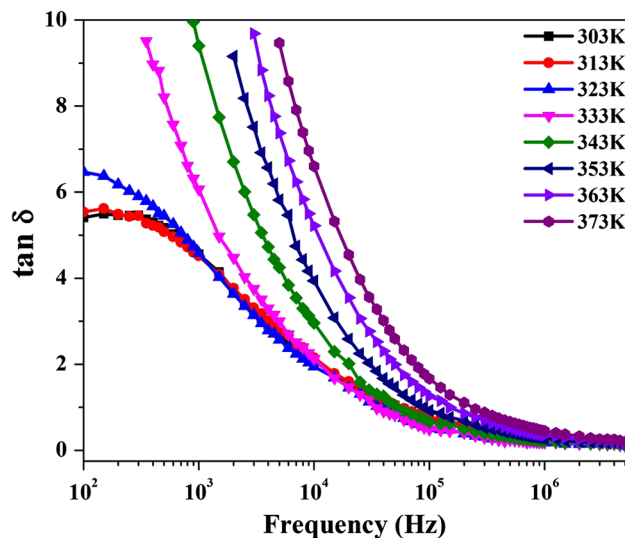
lower frequency region, the high value of the dielectric loss is due to the low conducting phase of grain boundaries which signifies more energy required for electron exchange between the Mn^{3+} and Mn^{4+} ions indicating maximum energy loss. The low value of the dielectric loss observed with the increase in frequency. As a result, a small amount of energy is sufficient for electron exchange. As temperature increases, the high value of the dielectric loss is seen at the lower frequency which is due to thermally activated charges and accumulation of charge carriers at the interfaces [19, 20].

3.3 Impedance studies

The frequency and temperature dependent real (Z′) and imaginary (Z″) part of impedance is calculated using the equation given below.

$$Z' = G/\left(G^2 + \omega^2 C_p^2\right) \quad \text{and} \quad Z'' = \left(\omega C_p/G^2 + \omega^2 C_p^2\right),$$

(5)

where G is the conductance (S), C_p is the static capacitance in parallel equivalent circuit mode (F) of the material.

Variation in the real part of impedance (Z′) with frequency for different temperature is shown in Fig. 6. It observed that the real part (Z′) of impedance remains constant at lower frequency region, and merging of Z′ occurs for various temperatures with the increase in frequency that is due to the space charge effects. It was also observed that the real part of impedance Z′ decreases with increase in temperature denoting the lower density of trapped charges and enhancement of the immobile species at lower frequency [21].
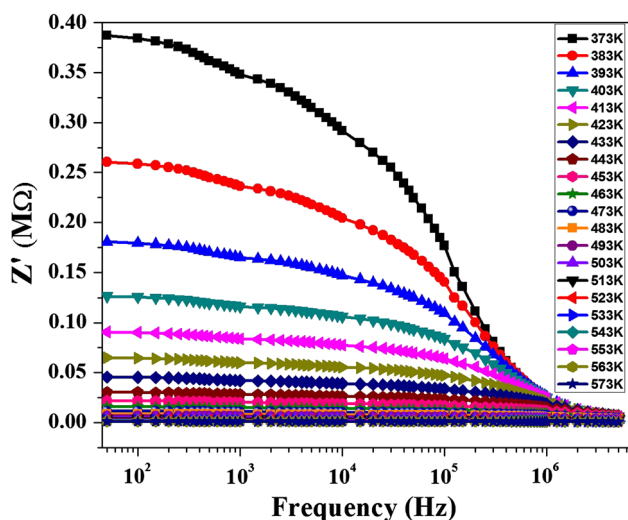
Fig. 6 Variation of real part of impedance (Z′) with frequency for different temperatures

Figure 7a shows the variation of imaginary part (Z″) of impedance with frequency for different temperatures. It clearly observed from Fig. 7a that the peak decreases and shift's towards the higher frequency with the increase in temperature denoting the temperature dependent relaxation process in the material. Usually, the relaxation process in oxide materials is due to the presence of oxygen vacancy. At lower temperature the relaxation process is due to the oxygen vacancy and higher temperature as a result of defects in the material. The relaxation time for the imaginary part of impedance is obtained from the maxima peak using the formula

$$\tau = 1/2\pi f_{max}, \tag{6}$$

Arrhenius equation to calculate the activation energy is

$$\tau = \tau_0 e^{E_a/K_B T}, \tag{7}$$

where τ_0 is the pre-exponential factor, E_a is activation energy, K_B is Boltzmann constant, and T is temperature. Arrhenius plot for temperature dependent relaxation time is shown in Fig. 7b. The activation energy (E_a) obtained is 1.2061 eV that is in good agreement with the absolute value of activation energy of 1.2 eV [9, 22]. However, this value attributes to the grain bulk and grain boundary conduction. This value of activation energy is due to the depletion in the oxygen vacancies at the adjacent space charge regions of the grain boundaries and also due to the hopping mechanism between Mn^{3+} and Mn^{4+}.

Nyquist plots of the impedance spectra at different temperature for $ZnMn_2O_4$ are shown in Fig. 8a, b. It is one of the influential techniques to analyze the electrical properties with individual contribution from the grains, grain boundaries and interface effects over a wide range of
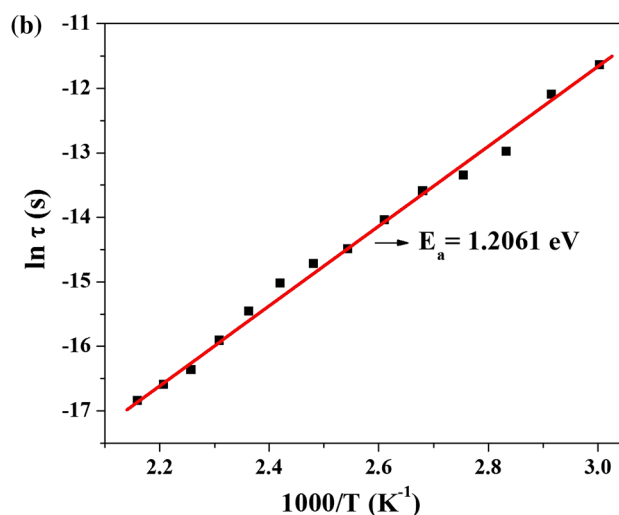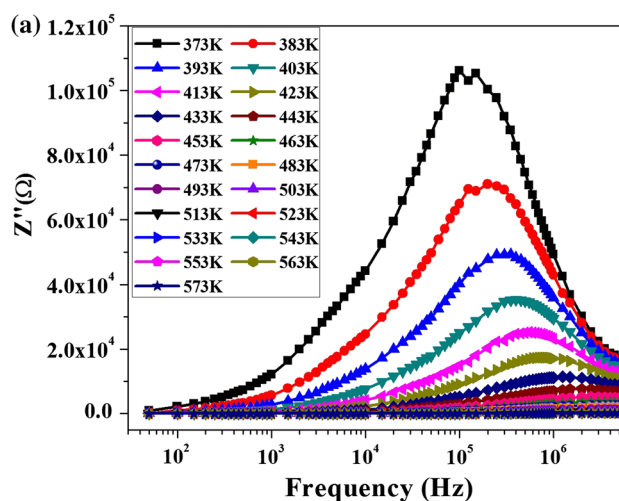

Fig. 7 a Variation of imaginary part of impedance (Z″) with frequency for different temperatures, **b** Arrhenius plot of temperature dependence of relaxation time from variation of imaginary part (Z″) of impedance with frequency

frequency. Nyquist plot consists of one or two semicircles depending upon the property of the material. The semicircle at the lower frequency is due to the grain boundary and the same at high frequency is due to grain conduction. It observed from the Fig. 8a that the impedance spectra for the temperature ranges from 363 to 423 K clearly shows the overlapping of two semicircles with a spike attached to it which signifies the grain and grain boundaries resistances and spikes to the interfacial effects. Impedance plot for temperatures from 403 to 423 K in Fig. 8a shows the single semicircle with a spike attached attributing to the dominance of grain resistance in the material. Nyquist plot shown in the Fig. 8b indicates the single semicircle of grain resistance along with the grain boundary resistance effect which is very small, as there are no clear semicircles but a spike attached to the semicircle. From the Nyquist plot, it is
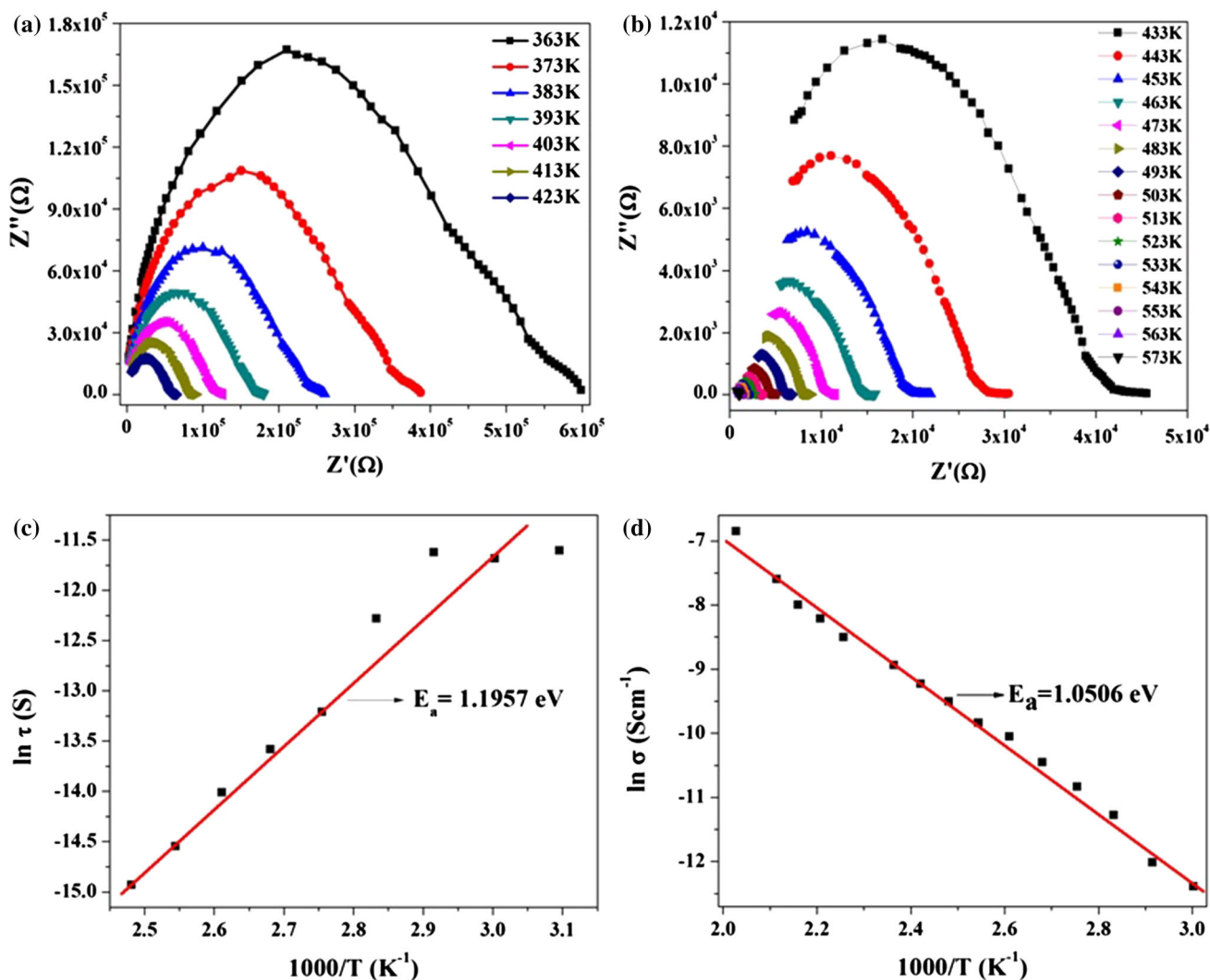
Fig. 8 a, b Nyquist plot of impedance data for different temperatures, **c** Arrhenius plot of temperature dependence of relaxation time from Nyquist plot and **d** ln σ versus 1000/T

observed that the centre of the semi-circle is depressed with the rise in temperature signifying the decrease in the impedance value which influences the conductivity and which results in the thermal activation of the material [23]. It also confirms the decrease in the grain and grain boundary resistance of the material with the increasing temperature which attributes to the behaviour of negative temperature co-efficient of resistance for NTC thermistor applications. The value of grain resistance (R_g), grain capacitance (C_g) and relaxation time (τ_g) are calculated from the Nyquist plot. Further, activation energy calculated from the Arrhenius equation for the relaxation time that is shown in the Fig. 8c. Activation energy (E_a) is found to be 1.1957 eV that is again in good agreement with the existence of oxygen vacancy and defects in cations that obtained from the imaginary part of impedance (Z'') [10]. Ionic conductivity of the material is obtained using the

grain resistance (R_g) concerning rise in temperature by the formula

$$\sigma = d/R_g S, \tag{8}$$

where σ is ionic conductivity, d is the thickness of the pellet and S is the surface area of the pellet. Figure 8d shows the ionic conductivity against 1000/T plot where it observed that the ionic conductivity increases with increase in temperature and activation energy obtained to be 1.0506 eV. This activation energy corresponds to the diffusion of oxygen vacancies as well as the oxygen vacancy complexes or defect dipoles [9].

3.4 Electrical modulus

The values of real (M') and imaginary (M'') part of electrical modulus is calculated using the relation

$$M' = \omega C_0 Z'' \quad \text{and} \quad M'' = \omega C_0 Z', \qquad (9)$$

where M' and M'' are real and imaginary part of the electric modulus, $C_0 (= \varepsilon_0 A/d)$ is the vacuum capacitance of the measuring pellet and the pellet thickness d, area of cross-section A, the permittivity of free space ε_0, and the angular frequency ω. Figure 9 shows the variation of real part of the electric modulus (M') with frequency for different temperatures of $ZnMn_2O_4$. It observed that the minimal value of M' for all temperature at lower frequency region signified the temperature independence in the real part of modulus and consequent dispersion with increasing frequency for all temperatures. This behaviour indicates the suppression in the electrode polarization effect at lower frequency region [24].

Figure 10a shows the imaginary part of the electric modulus (M'') with frequency for different temperatures. The shift in the peak of the modulus towards the higher frequency for higher temperature signifies that the relaxation is thermally activated in the material and also confirms the earlier discussions on relaxation. Also, the asymmetric broadening of the modulus peaks denotes the spreading of relaxation time and non-Debye type of relaxation [25]. The Arrhenius plot of the temperature dependence of relaxation time for variation in M'' with frequency shown in Fig. 10b. The activation energy obtained is 1.14506 eV that is in the range of the oxygen vacancy justifying the earlier discussion on the material. This result in the diffusion of oxygen vacancies as well as the defect dipoles or oxygen vacancy complexes composed of oxygen and other cation vacancies. In this material the hopping between Mn^{3+} and Mn^{4+} also creates oxygen vacancy that results in the relaxation process.
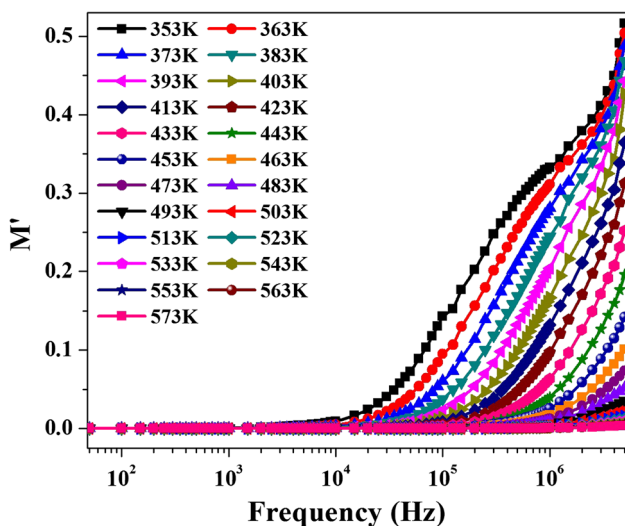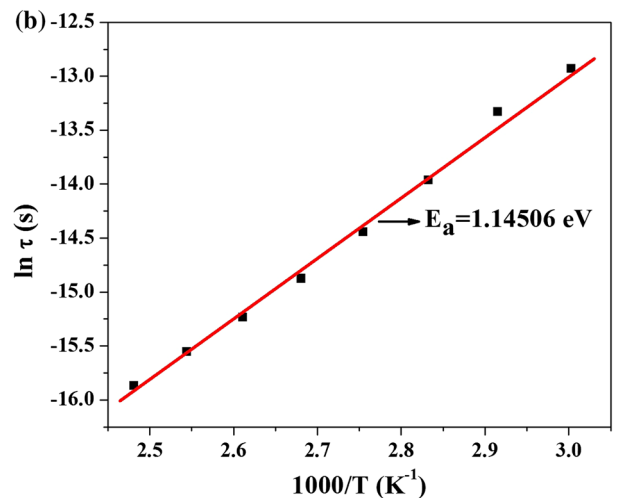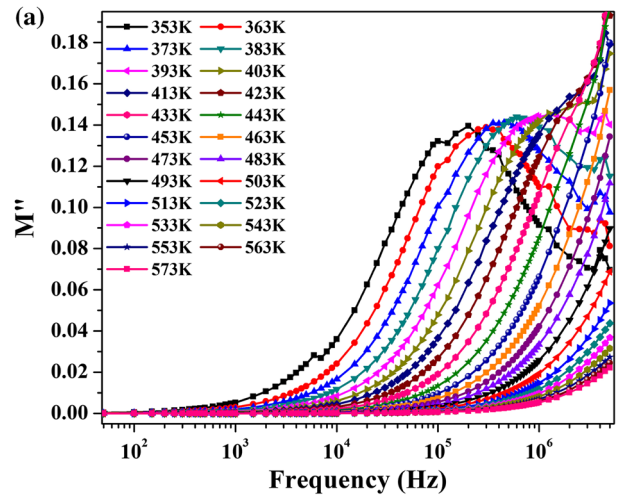
Fig. 10 **a** Variation of imaginary part of electric modulus (M'') as a function of frequency for different temperatures from 353 to 573 K, **b** Arrhenius plot of temperature dependence of relaxation time from variation of (M'') with frequency

Fig. 9 Variation of real part of electric modulus (M') as a function of frequency for different temperatures
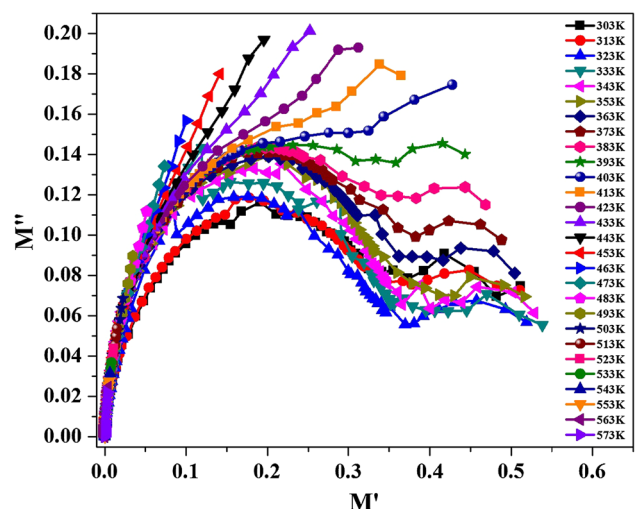
Fig. 11 Complex electrical modulus plot for different temperatures of $ZnMn_2O_4$

Complex electric modulus explains the difference between grains, grain boundary and electrode polarization effect in the material. Figure 11 shows the complex modulus plot for various temperatures. At lower temperature, it clearly shows the two semicircles indicating the grain and grain boundary conduction in the material that gradually suppresses denoting demolition of the grain boundary effect in the material. At higher temperature hopping of ions within the Mn site results in the suppression of semicircular arc into an arc [26].

4 Conclusion

Nanocrystalline $ZnMn_2O_4$ material was synthesized by the sol–gel method by using glycine as a chelating agent with microwave assisted sintering. XRD pattern clearly confirmed the formation of tetragonal $ZnMn_2O_4$ with the space group I41/amd. SEM image showed the grain and grain boundaries in the synthesized material. The existence of grain boundaries, defects, hopping of electrons between Mn^{3+} and Mn^{4+}, oxygen vacancy and space charge polarization effect played a major role in the dielectric relaxation. The impedance and electric modulus studies as a function of frequency for different explained the strong correlation between the grains and grain boundaries. Detailed studies of impedance and modulus have provided insight into the electrical properties and relaxation process in the material. The activation energy was obtained using Arrhenius plot under different perspectives of impedance and modulus. It confirmed the existence of the oxygen vacancies in the adjacent space charge regions of the grain boundaries and also due to the hopping mechanism between Mn^{3+} and Mn^{4+}. Nyquist plot of impedance confirms the reduction in the resistance with increasing temperature, which further signifies its potential application as NTC thermistor.

References

1. R. Gherbi, Y. Bessekhouad, M. Trari, Structure, optical and transport properties of Mg-doped $ZnMn_2O_4$. J. Alloys Compd. **655**, 188–197 (2016). doi:10.1016/j.jallcom.2015.09.192
2. P. Zhang, X. Li, Q. Zhao, S. Liu, Synthesis and optical property of one- dimensional spinel $ZnMn_2O_4$ nanorods. Nanoscale Res. Lett. **6**, 323 (2011). doi:10.1186/1556-276X-6-323
3. S.V. Lakshmi, S. Pauline, Structural, morpological and optical properties of hetarolite—$ZnMn_2O_4$ nano particle by hydrothermal method. Int. J. Sci. Res. **3**, 8–9 (2014)
4. Y. Deng, S. Tang, Q. Zhang, Z. Shi, L. Zhang, S. Zhan et al., Controllable synthesis of spinel nano-$ZnMn_2O_4$ via a single source precursor route and its high capacity retention as anode material for lithium ion batteries. J. Mater. Chem. **21**, 11987 (2011). doi:10.1039/c1jm11575h
5. R.N. Jadhav, V. Puri, Effect of film thickness and pH of zinc manganite on microwave absorption and complex permittivity. Synth. React. Inorg. Met. Org. Nano-Met. Chem. **44**, 1426–1428 (2014). doi:10.1080/15533174.2013.809744
6. F. Méndez-martínez et al., $Zn_{x-1}Cu_xMn_2O_4$ spinels; synthesis, structural characterization and electrical evaluation. J. Mex. Chem. Soc. **54**(1), 2–6 (2010)
7. M. Khairy, M.A. Mousa, Electrical and catalytic properties of gamma-irradiated and unirradiated $ZnMn_2O_4$ nanoparticles. Am. J. Chem. **2**(6), 306–311 (2012)
8. J. Takahashi, A. Miura, H. Itoh, K. Sawayama, T. Akazawa, Phase change and electrical resistivity of Zn–Mn–Ni–O-based NTC thermistors produced using IZC powder recycled from used dry batteries. Ceram. Int. **34**, 853–857 (2008). doi:10.1016/j.ceramint.2007.09.035
9. C.C. Wang, C.M. Lei, G.J. Wang, X.H. Sun, T. Li, Oxygen-vacancy-related dielectric relaxations in $SrTiO_3$ at high temperatures. J. Appl. Phys. **094103**, 1–10 (2013). doi:10.1063/1.4794349
10. C. Elissalde, J. Ravez, Ferroelectric ceramics: defects and dielectric relaxations. J. Mater. Chem. (2001). doi:10.1039/b010117f
11. Y. Bessekhouad, M. Trari, Photocatalytic hydrogen production from suspension of spinel powders AMn_2O_4 (A = Cu and Zn). Int. J. Hydrogen Energy **27**, 357–362 (2002)
12. J. Xu, Z. Yang, Y. Zhang, X. Zhang, H.U.A. Wang, Bipolar resistive switching behaviours in $ZnMn_2O_4$ film deposited on p$^+$-Si substrate by chemical solution deposition. Bull. Mater. Sci. **37**, 1657–1661 (2014)
13. P. Li, J. Liu, Y. Liu, Y. Wang, Z. Li, W. Wu et al., Three-dimensional $ZnMn_2O_4$/porous carbon framework from petroleum asphalt for high performance lithium-ion battery. Electrochim. Acta **180**, 164–172 (2015). doi:10.1016/j.electacta.2015.08.095
14. C. Dong, PowderX: Windows-95-based program for powder X-ray diffraction data processing. J. Appl. Crystallogr. **32**(4), 838 (1999)
15. J. Langford II, A.J.C. Wilson, Scherrer after sixty years: a survey and some new results in the determination of crystallite size. J. Appl. Crystallogr. **11**(2), 102–113 (1978). doi:10.1107/S0021889878012844
16. N. Kumari, V. Kumar, S.K. Singh, Structural, dielectric and magnetic investigations on Al^{3+} substituted Zn ferrospinels. RSC Adv. **5**, 37925–37934 (2015). doi:10.1039/C5RA03745J
17. H. Rahmouni, M. Smari, B. Cerif, E. Dhahri, K. Khirouni, Conduction mechanism, impedance spectroscopic investigation and dielectric behavior of $La_{0.5}Ca_{0.5-x}Ag_xMnO_3$ manganites with the composition below the concentration limit of silver solubility in perovskites (0 < x<0.2). Dalton Trans. (2015). doi:10.1039/C5DT00444F
18. S. Singh, S.E. Shirsath, Structural phases and Maxwell–Wagner relaxation in magnetically soft-$ZnFe_2O_4$ and hard-$Sr_2Cu_2Fe_{12}O_{22}$ nanocomposites. Ceram. Int. (2015). doi:10.1016/j.ceramint.2015.10.023
19. O. Padmaraj, M. Venkateswarlu, N. Satyanarayana, Structural, electrical and dielectric properties of spinel type $MgAl_2O_4$ nanocrystalline ceramic particles synthesized by the gel-combustion method. Ceram. Int. **41**, 3178–3185 (2015). doi:10.1016/j.ceramint.2014.10.169
20. T. Javed, A. Maqsood, Structural, electrical and dielectric properties of Co–Mn spinel nanoferrites prepared by co-precipitation technique. J Supercond. Nov. Magn. **4**, 2137–2144 (2011). doi:10.1007/s10948-011-1168-7
21. C. Sujatha, K.V. Reddy, K.S. Babu, A.R. Chandra, M.B. Suresh, K.H. Rao, Effect of Co substitution of Mg and Zn on electromagnetic properties of NiCuZn ferrites. J. Phys. Chem. Solids **74**, 917–923 (2013). doi:10.1016/j.jpcs.2013.02.005

22. M. Gerstl, E. Navickas, M. Leitgeb, G. Friedbacher, F. Kubel, J. Fleig, The grain and grain boundary impedance of sol-gel prepared thin layers of yttria stabilized zirconia (YSZ). Solid State Ion. **225**, 732–736 (2012). doi:10.1016/j.ssi.2012.02.012

23. M. Gerstl, E. Navickas, G. Friedbacher, F. Kubel, M. Ahrens, J. Fleig, The separation of grain and grain boundary impedance in thin yttria stabilized zirconia (YSZ) layers. Solid State Ion. **185**, 32–41 (2011). doi:10.1016/j.ssi.2011.01.008

24. W. Chen, W. Zhu, C. Ke, Z. Yang, L. Wang, X.F. Chen et al., Impedance spectroscopy and conductivity mechanism of CoFe$_2$O$_4$–Pb(Zr$_{0.53}$Ti$_{0.47}$)O$_3$ composite thick films. J. Alloys Compd. **508**, 141–146 (2010). doi:10.1016/j.jallcom.2010.08.029

25. A. Mekap, P.R. Das, R.N.P. Choudhary, Dielectric, magnetic and electrical properties of ZnFe$_2$O$_4$ ceramics. J. Mater. Sci.: Mater. Electron. **24**, 4757–4763 (2013). doi:10.1007/s10854-013-1470-1

26. L.S. Lobo et al., Investigation of electrical studies of spinel FeCo$_2$O$_4$ synthesized by sol-gel method. Superlattices Microstruct. (2015). doi:10.1016/j.spmi.2015.09.010